Multiscale simulation of thrombus growth and vessel occlusion triggered by collagen/tissue factor using a data-driven model of combinatorial platelet signalling

Yichen Lu, Mei Yan Lee, Shu Zhu, Talid Sinno and Scott L. Diamond*

Department of Chemical and Biomolecular Engineering, Institute for Medicine and Engineering, University of Pennsylvania, Philadelphia PA 19104, USA
*Corresponding author: Email: sld@seas.upenn.edu

During clotting under flow, platelets bind and activate on collagen and release autocrinic factors such as ADP and thromboxane, while tissue factor (TF) on the damaged wall leads to localized thrombin generation. Towards patient-specific simulation of thrombosis, a multiscale approach was developed to account for: platelet signalling [neural network (NN) trained by pairwise agonist scanning (PAS), PAS-NN], platelet positions (lattice kinetic Monte Carlo, LKMC), wall-generated thrombin and platelet-released ADP/thromboxane convection–diffusion (partial differential equation, PDE) and flow over a growing clot (lattice Boltzmann). LKMC included shear-driven platelet aggregate restructuring. The PDEs for thrombin, ADP and thromboxane were solved by finite element method using cell activation-driven adaptive triangular meshing. At all times, intracellular calcium was known for each platelet by PAS-NN in response to its unique exposure to local collagen, ADP, thromboxane and thrombin. When compared with microfluidic experiments of human blood clotting on collagen/TF driven by constant pressure drop, the model accurately predicted clot morphology and growth with time. In experiments and simulations at TF at 0.1 and 10 molecule-TF/μm^2 and initial wall shear rate of 200 s^{-1}, the occlusive blockade of flow for a 60-μm channel occurred relatively abruptly at 600 and 400 s, respectively (with no occlusion at zero TF). Prior to occlusion, intrathrombus concentrations reached 50 nM thrombin, ~1 μM thromboxane and ~10 μM ADP, while the wall shear rate on the rough clot peaked at ~1000–2000 s^{-1}. Additionally, clotting on TF/collagen was accurately simulated for modulators of platelet cyclooxygenase-1, P2Y$_1$ and IP-receptor. This multiscale approach facilitates patient-specific simulation of thrombosis under hemodynamic and pharmacological conditions.

Keywords: platelet aggregation; multiscale modelling; thrombosis; thrombin; stenosis.

1. Introduction

Platelets play a critical role in primary haemostasis to prevent blood loss due to vessel injury. Secondary haemostasis requires tissue factor (TF) to activate the coagulation protease cascade leading to thrombin generation and subsequent fibrin polymerization to stabilize the clot. Unfortunately, during atherosclerotic plaque rupture that initiates a heart attack, flowing blood is exposed to a highly procoagulant surface containing TF. Platelets are captured from flow and activate on collagen. Intracellular calcium mobilization results in integrin activation and firm arrest, dense granule release of Adenosine diphosphate (ADP), activation of cycloxygenase-1 (COX1) with consequent thromboxane (TXA$_2$) synthesis, and phosphatidylserine exposure. Both ADP and TXA$_2$ are autocrinic species that enhance platelet activation and are highly targetable by drugs (e.g. P2Y$_{12}$ inhibitors and aspirin) to reduce risk.

Thrombosis is the result of complex biological processes that occur in space and time and are coupled to prevailing hemodynamic that dictate cell collision rates, dilution of reactive species and forces on clot ensembles. Computational modelling of thrombosis has advanced significantly (Xu *et al.*, 2008; Leiderman & Fogelson, 2011; Sweet *et al.*, 2011; Flamm *et al.*, 2012; Xu *et al.*, 2012; Wu *et al.*, 2014; Babushkina *et al.*, 2015; Tosenberger *et al.*, 2016) as reviewed by Diamond (2013) and Fogelson & Neeves (2015). The opportunity now exists to use patient-specific hemodynamic (Taylor *et al.*, 2013), platelet signalling models (Chatterjee *et al.*, 2010; Flamm *et al.*, 2012; Lee & Diamond, 2015), and bottom-up models of coagulation (Hockin *et al.*, 2002; Chatterjee *et al.*, 2010) for multiscale simulations of thrombosis (Flamm *et al.*, 2012). Such multiscale simulations can be compared and validated against direct measurements of clotting reactions over defined reactive surfaces and shear rates in microfluidic flows (Maloney *et al.*, 2010; Colace *et al.*, 2012; Zhu *et al.*, 2015).

In prior work (Flamm *et al.*, 2012), a multiscale platelet deposition model utilized a four-agonist (ADP, TXA_2, collagen, prostacyclin) neural network (NN) to predict platelet dynamics under venous and arterial shear condition in the absence of thrombin. This NN was trained using calcium traces obtained for all single and pairwise combinations of agonists at low, medium and high concentration. In this pairwise agonist scanning (PAS) experiment, ADP and mimetics for collagen, thromboxane, and prostacyclin were used to quantify $P2Y_1/P2Y_{12}$, GPVI, TP and IP signalling, respectively, for NN training. Along with NN for platelet signalling, the multiscale platelet deposition model utilized a velocity field solved by lattice Boltzmann (LB) and prevailing concentration profiles obtained by finite element (FEM) solution of convection–diffusion PDEs. Platelet motion and binding/unbinding were solved stochastically by the LKMC method.

In this study (Figs 1 and 2), the multiscale model has been expanded and refined in several important aspects: (i) the NN prediction of platelet calcium was expanded to include thrombin in the PAS training set averaged over 10 healthy donors (50% male) (Lee & Diamond, 2015); (ii) the FEM mesh for solution of ADP, TXA_2 and thrombin spatiotemporal concentrations was adaptively refined based on platelet activation (Figs 3 and 4); (iii) individual platelets were allowed to find the most stable nearby position of greatest bonding after initial capture to the clot (Figs 5 and 6); (iv) thrombin was released from the wall into the clot assuming a parameterized curve with initiation and decaying stages (Fig. 7); and (v) flow fields were calculated for either constant flow rate (non-physiologic but experimentally accessible) or constant pressure-drop (full channel occlusion possible) (Supplementary Fig. S1).

The adaptive meshing algorithm allowed for efficient calculation of soluble species transport with ongoing platelet capture and activation. The remodelling algorithm was embedded in the LKMC model to achieve more realistic clot morphologies. The simulated platelet deposition results were compared with two different modes of microfluidic experiments (the constant flow and pressure relief mode) (Muthard & Diamond, 2012). In the constant flow mode, blood was perfused at constant flow rate through a microfluidic device where growing platelet deposits experience increasingly high shear as the clot grows across the channel. In the pressure relief mode (Supplementary Fig. S1), flow was diverted from the occluding channel to an open non-clotting channel so that clots were able to grow completely across the channel until flow stopped. The multiscale model accurately simulated the platelet morphology and clot growth rates observed in the two different modes and provided quantitative predictions on platelet deposition dynamics consistent with experiments with healthy human blood treated with the Factor XIIa inhibitor, corn trypsin inhibitor (CTI).

To our knowledge, this is the first model to quantitatively predict dynamic platelet deposition in the presence of wall-generated thrombin and inhibitors of ADP or thromboxane, as validated by comparison with actual data obtained with flowing human blood. Such predictions are novel and relevant given the clinical use of direct thrombin inhibitors and antiplatelet agents targeting ADP and thromboxane
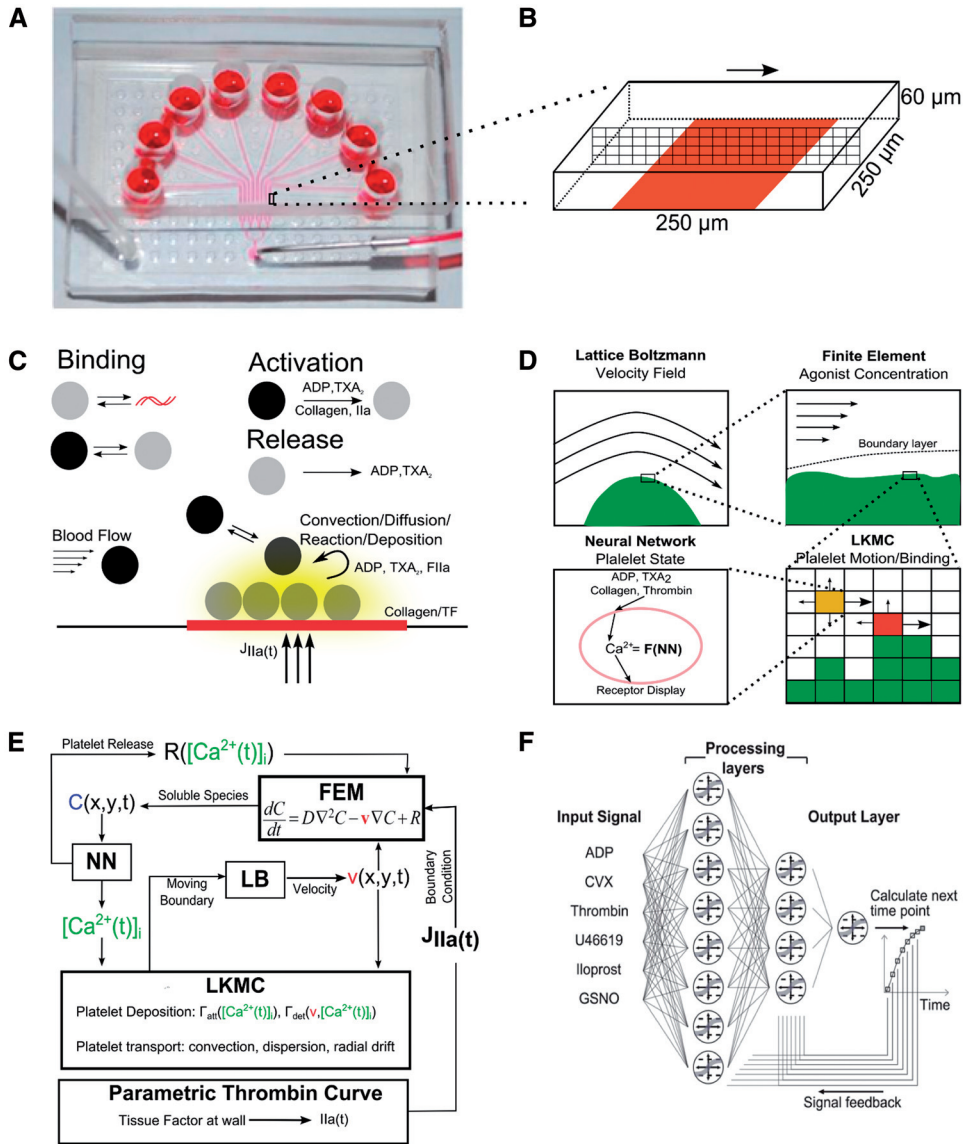
FIG. 1. Multiscale model of platelet activation and thrombus formation under flow. An 8-channel microfluidic device allows whole blood perfusion through each high aspect ratio channel (250 μm wide × 60 μm high) and over a discrete 250 μm-long collagen patch (a). A 2D multiscale model domain (500 μm long × 60 μm high) corresponds to the centre of the microfluidic channel which includes collagen as a uniform boundary (b). The biology and physics of thrombosis includes flowing platelets being captured to collagen or other bound platelets, platelet activation triggered by collagen (*rectangular bar at bottom*) and thrombin (Factor IIa, FIIa) modelled as a boundary condition [time-dependent flux $J_{FIIa}(t)$] and ADP/TXA$_2$, which are autocrinic molecules released by platelets reaching a critical level of activation (c). The multiscale simulation of platelet deposition under flow requires simultaneous solution of the instantaneous velocity field v over a complex and evolving platelet boundary by LB, concentration profiles of ADP, TXA$_2$ thrombin by FEM, individual intracellular platelet state ([Ca^{2+}]$_i$) dictated by NN model and activation-dependent release reactions R for ADP and TXA$_2$, and all platelet positions and adhesion/detachment kinetics by LKMC (d, e). A 2-layer, 12-node NN architecture was employed for prediction of intracellular calcium in response to agonist exposure. Agonist concentrations at a given time point were fed into the processing layers. The layers then integrated the input signal with feedback at t = 1, 2, 4, 8, 16, 32, 64 and 128 s to calculate [Ca^{2+}]$_i$ at the next time point (f) (for related colour see the online version).
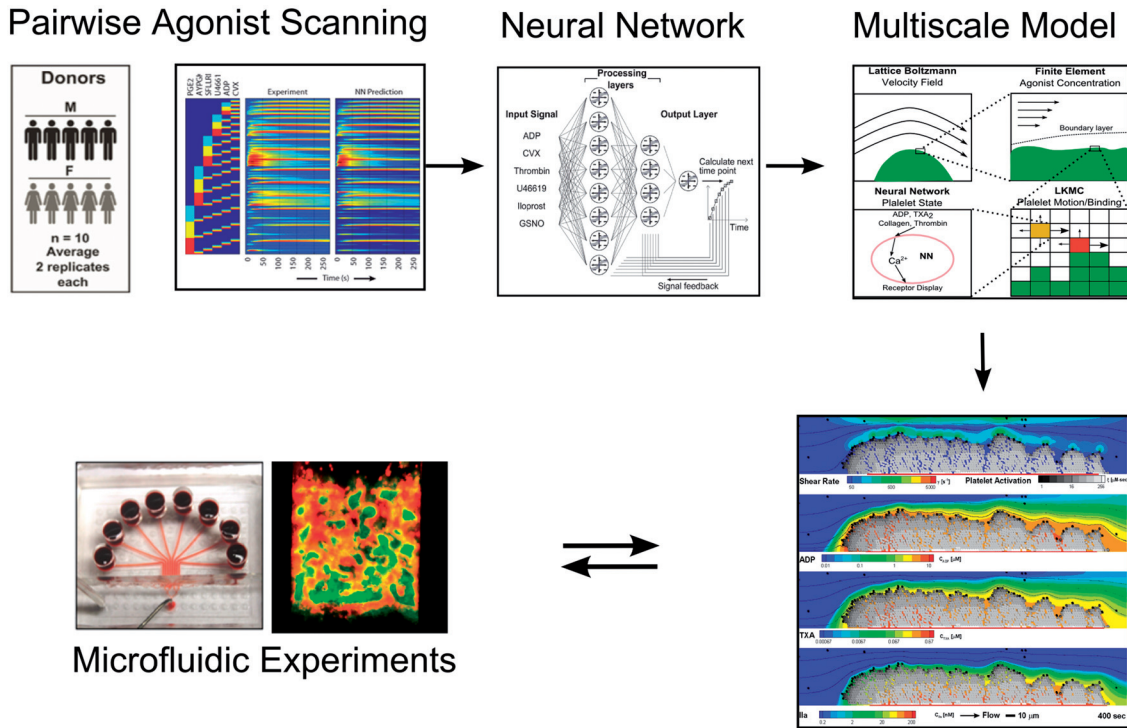
FIG. 2. Connection between experimental measurement and numerical prediction. PAS experiments were performed on 10 healthy donors (50% male) to train a NN ensemble with 6160 calcium traces to predict calcium response for an average healthy person and was incorporated into the multiscale model to predict platelet activation. An effective boundary flux term was imposed. Thrombus growth dynamics can be predicted by the multiscale model and were compared against microfluidic experiments on healthy human blood conducted under identical conditions.

autocrinic signalling. While other models have predicted dynamic platelet deposition in the presence of thrombin generation (Xu *et al.*, 2010; Leiderman & Fogelson, 2011), to our knowledge, this is the first model to include inhibitors of ADP and thromboxane, agonists of the IP receptor, and be directly compared with experimental data. To our knowledge, this is also the first study to quantitatively predict platelet-mediated channel occlusion and to compare predicted occlusion times to actual measurements conducted under constant pressure drop conditions. Additionally, the model predicts a peak thrombin flux on the order of 10^{-12} nmole/μm^2-s testable by experimental measurement for a TF rich surface exposed to flowing blood.

2. Methods

A 2D rectangular simulation domain (500 μm long × 60 μm high) was used for all simulations (Fig. 1b). At a location between 100 and 350 μm downstream of the simulation domain entrance, a 250-μm collagen patch was defined as a boundary condition (Fig. 1b and c). The 2D computational domain represented a centreline cross-section of an actual 3D microfluidic channel (250 μm wide × 60 μm high) used to perform the *ex vivo* whole blood perfusion experiments (Fig. 1a).
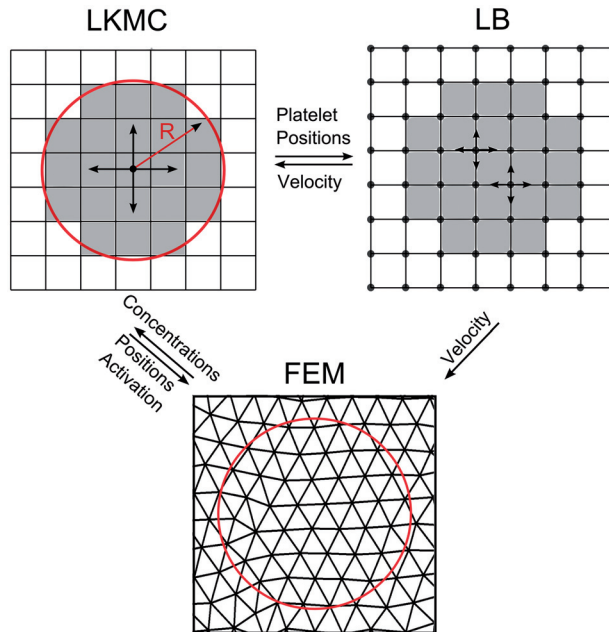
FIG. 3. Simulation domains and meshes for the different modules. In LKMC, each platelet (*in circle*) is resolved with multiple square elements (lattice spacing of 0.5 μm). In LB, the uniform grid had the same lattice spacing as LKMC, but was offset by 0.25 μm in each direction such that the LB nodes surround the LKMC pixels. In FEM, a refined triangular mesh was generated around the clotting region such that each platelet occupies ∼30 triangular elements. LKMC feeds platelet information such as position and activation states into LB and FEM. FEM computes concentration field for soluble species interpolated back onto the LKMC grids. LB computes the velocity field used by both FEM and LKMC (for related colour see the online version).

The overall computational framework utilized four coupled modules. At the centre of the framework, a LKMC simulator was used to evolve platelet positions in time on a regular square grid. Platelets were assumed to be rigid circular particles with diameter of 3 μm. The LKMC simulation was informed by three other computational modules (Fig. 1d–f) to fully specify rates for the various platelet events (e.g. translation, binding, unbinding). First, the velocity field that convects the platelets across the microchannel from entrance to exit was computed with the LB method. The LB simulation assumes a quasi-steady flow profile that depends on the instantaneous thrombus boundary location and is resolved at a resolution approaching the single platelet scale. Next, the concentration profiles of the soluble platelet agonists (ADP, TXA$_2$ and thrombin) were described by a system of convection–diffusion-reaction equations that were solved using finite element method (FEM). Finally, the activation state of each platelet, as defined using a metric based on intracellular calcium $[Ca^{2+}(t)]_i$ was calculated in time using the NN model for the unique multicomponent agonist exposure experienced by each platelet. The connectivity between these various computational modules is shown in (Fig. 1d and e). Each of the four computational modules are described in detail in the following sections.

2.1 NN module

PAS was used to obtain calcium traces for apixaban-treated, diluted and calcium dye-loaded platelet rich plasma (PRP) stimulated with all single and pairwise combinations of six different agonists used at low,
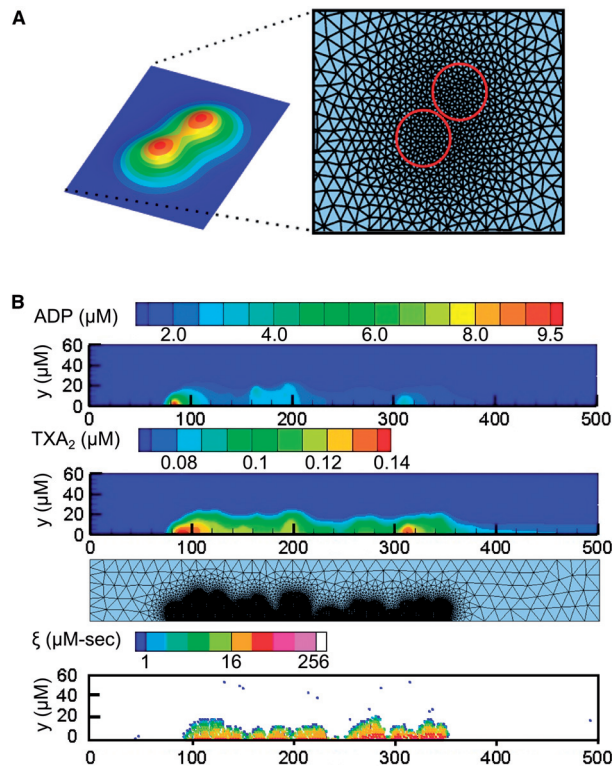
FIG. 4. Platelet activation-driven adaptive triangular meshing. The 2D Gaussian influence function and the resultant meshes for an example case of two adjacent and activated platelets (a). The triangular mesh is shown for a typical thrombus configuration and the resultant concentration fields for ADP and TXA$_2$ as well as each platelet's activation state of integrated intracellular calcium (b).

medium and high concentrations (0.1, 1 and 10 × EC$_{50}$) (Chatterjee *et al*., 2010). In this approach, the six agonists used were: ADP, U46619 (thromboxane mimetic), convulxin (collagen mimetic), thrombin, GSNO (NO donor) and iloprost (prostacyclin analog). NN training was then carried out using the NN Toolbox in the MATLAB software package to predict platelet calcium level for any agonist dose and combination. Output concentrations were mapped between 0 (resting calcium levels) and 1 (maximal response). The structure of the *NARX* (Nonlinear AutoRegressive network with eXogenous inputs) model utilized two-layer processing (eight nodes in the first layer and four nodes in the second layer) and a tapped delay line with 128 s of feedback to each layer (Fig. 1f). The hyperbolic tangent transfer function was used in all nodes and a linear transfer function was used in the output layer. Initial states of the feedback were set to 0 corresponding to the resting platelet. The NN predicted the calcium level for the next time step based on the feedback vector (1, 2, 4, 8, 16, 32, 64 and 128 s prior to the current instant) and the current concentration input from the six agonists. A 100 NN-ensemble for PAS of 10 healthy donors and 10 trained NNs per donor predicted averaged calcium concentration output for human platelets exposed to any combinations of the six agonists. This approach captured the measured information from 6160 calcium traces containing 511,280 calcium data points. See Lee & Diamond (2015) for detailed information validating PAS-NN prediction of [Ca^{2+}(*t*)]$_i$ beyond the pairwise training set for trinary stimulations, 4–6 agonist stimulations and sequential agonist stimulations.
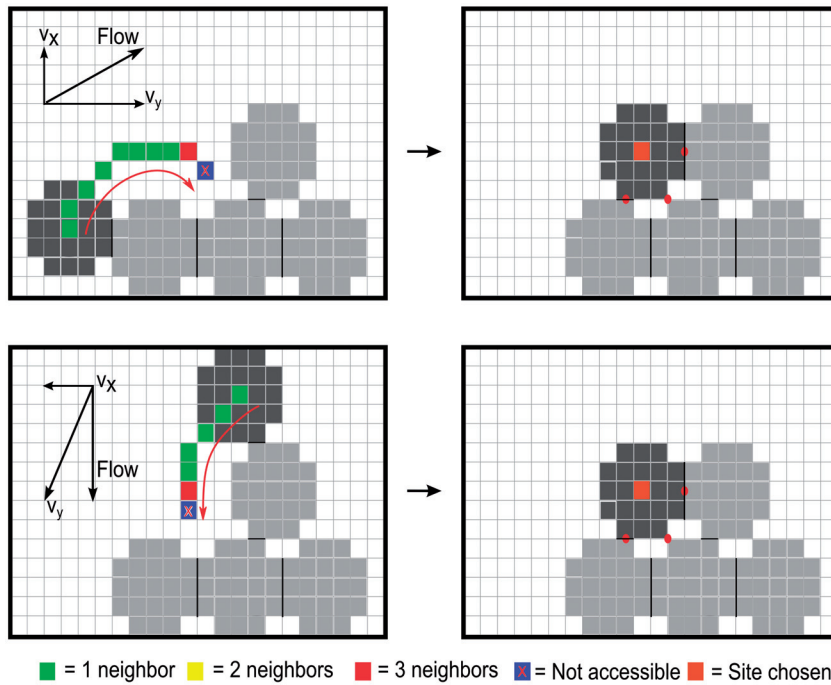
FIG. 5. Remodelling algorithm for platelet deposition. Upon binding, the number of contacts the adhering platelet experiences (colour coded at each cell centre position along the trajectory) is calculated until forbidden overlap is achieved, whereby the most favourable binding site was chosen based on the cumulative potential binding rates.
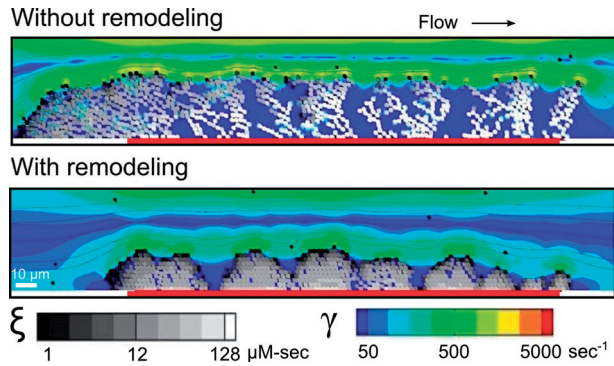
FIG. 6. Comparison of thrombus morphology with and without the remodelling algorithm. The remodelling algorithm resulted in physically realistic clot morphology (*bottom*) as compared to the highly dendritic and mechanically unlikely structure obtained without remodelling upon adhesion (*top*).

2.2 *LB for blood flow*

The LB method was used to solve the flow field around the platelets satisfying the incompressible Navier–Stokes equation with continuity condition. A D2Q9 scheme with Zou–He Boundary conditions

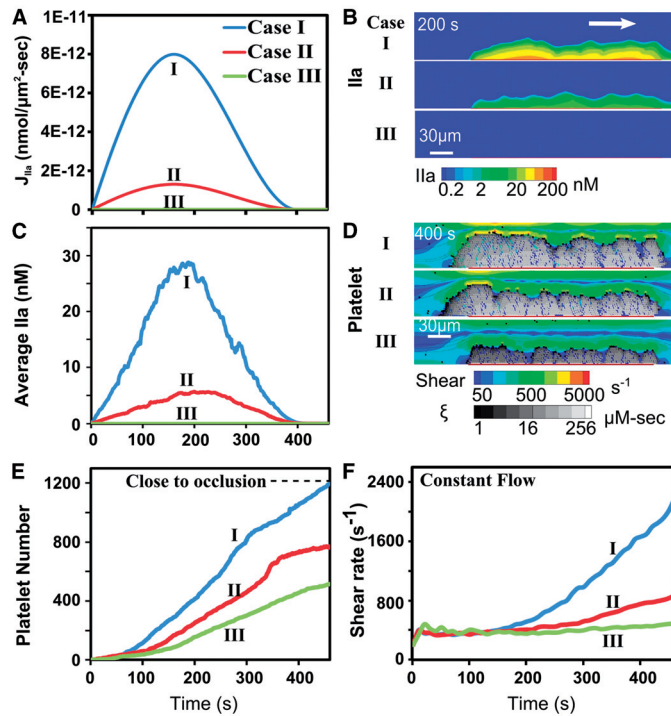Fig. 7. Comparison of different thrombin flux signals for constant flow rate simulations at initial inlet wall shear rate $= 200$ s^{-1}. Different thrombin flux conditions were imposed on the wall. Case I represents normal physiological condition ($T_{max} = 160$ s, $J_{max} = 8E-12$ nmol/μm^2) under high TF stimulation. Case II has a five-fold reduction in J_{max}. Case III shows a base case with zero thrombin. (a) Thrombin boundary layer for three cases at 200 s. (b) Averaged thrombin for the thrombus as a function of time for three cases. (c) Snapshots of fully-developed thrombus configuration at 400 s for three different cases. (d) Comparison of platelet accumulation dynamics for three different cases. (e) Averaged shear rate at the outmost layer of platelets for three different cases. (f)

was applied (Zou & He, 1997). The top and bottom walls were treated as no-slip surfaces. Platelets were simulated as pixelated objects on the LKMC lattice (Fig. 3). Free flowing platelets and their interactions with each other were ignored in the LB model of Newtonian blood flow. However, the hydrodynamic effect of a clot-bound platelet on the fluid was explicitly handled in the LB model as a no-slip surface. Two different experimental settings, constant flow rate mode and pressure relief mode, were simulated. In the constant flow rate mode, blood was perfused over the microfluidic channel at a constant flow rate regardless of the size of the developing platelet deposit on the wall. In the pressure relief mode (Supplementary Fig. S1), two identical channels in parallel with a single outlet were perfused. Only one channel experienced obstruction caused by deposited platelets, while the other channel had no wall deposit (EDTA-treated blood in the real experiment). With increasing flow resistance caused by platelet accumulation, flow was diverted to the free channel which eventually led to zero flow in the fully obstructed channel. In the constant flow rate mode, a parabolic flow profile with initial wall shear of 200 s^{-1} was maintained at the inlet. In the pressure relief mode, a similar parabolic flow allowing the same wall shear for both of the two channels was maintained at the outlet.

2.3 *FEM for soluble agonist transport and reaction*

The concentration fields of the agonists, $C_j(x, y, t)$ for $j =$ ADP, TXA$_2$ and thrombin were obtained by solving a system of convection–diffusion-reaction equations using the FEM:

$$\frac{\partial C_j}{\partial t} + \mathbf{v} \cdot \nabla C_j = D_j \nabla^2 C_j + R_j, \tag{1}$$

where D_j was the Brownian diffusion coefficient of ADP, TXA$_2$ and thrombin, and $\mathbf{v}$ was the fluid velocity provided by the LB module. The release of ADP and TXA$_2$ by the ith platelet was triggered by its internal activation state, $\xi_i(t) = \int_0^t ([\text{Ca}_i] - [\text{Ca}]_{\text{baseline}})\, d\tau$ exceeding a critical level of $\xi_{\text{crit}} = 9\,\mu\text{ms}$. Once sufficiently activated, the platelet released ADP and TXA$_2$ with rates governed by an exponential decay function,

$$R_j(t) = \frac{M_j}{\tau_j} \exp\left(-\frac{t - t_{\text{release}}}{\tau_j}\right), \tag{2}$$

where M_j was the total moles of species j for a platelet and τ_j was a time constant. Published experiments have determined that each platelet can release 1×10^{-8} nmol of ADP with a time constant of 5 s (Holmsen *et al.*, 1972; Hubbell & McIntire, 1986) and 4×10^{-10} nmol of TXA$_2$ with a time constant of 100 s (De Caterina *et al.*, 1984). The element at the centre of the activated platelet was treated as the source element for the PDE calculation (FEM). Agonists were assumed to undergo transport by diffusion within the platelet mass.

2.4 *Thrombin release modelled as boundary flux*

Motivated by the work of Kuharsky & Fogelson (2001) and numerous observations of a thin thrombin/fibrin core that is immediately adjacent to wall-derived TF (Colace *et al.*, 2012; Welsh *et al.*, 2012, 2014; Muthard & Diamond, 2013; Stalker *et al.*, 2013, 2014; Tomaiuolo *et al.*, 2014), thrombin was introduced into the computational domain as a time-dependent wall boundary flux condition (Figs 1 and 2). This boundary flux assumption is consistent with a fixed amount of Factor X (FX) being activated to FXa near the wall due to extreme transport limits on FX diffusion through a dense and activated platelet aggregate since FX binds to activated platelets (Hathcock *et al*, 2007). Instead of resolving the full detail of the coagulation cascade, which involves ~50 PDEs and ~100 reactions where many of reaction kinetics has yet to be verified experimentally within dense platelet deposits formed under flow, thrombin was simulated as an imposed boundary flux at the wall with an initiation phase followed by a decay phase whose shape and peak value was motivated from both calibrated automated thrombography (CAT) and a previously validated ODE model (Chatterjee *et al.*, 2010).

Since measurements are not available for intrathrombus thrombin generation per molecule of TF on a surface, a 400-s thrombin flux profile (J, nmole/µm^2-s) was studied parametrically in three cases. *Case I*: strong thrombin flux for high [TF]$_{\text{wall}} = 10$ molecule-TF/µm^2; *Case II*: weak thrombin flux for low [TF]$_{\text{wall}} = 0.1$ molecule-TF/µm^2; and *Case III*: zero thrombin flux for TF-free wall condition. A two-piece cubic spline (8 degrees-of-freedom) for the thrombin flux was defined for the initiation and decay phases with the following imposed constraints: zero flux at the initial and final time of 400 s, continuity, slope and curvature matching at the joint, and zero slope at the final time. These constraints reduce the degrees-of-freedom to only two parameters: time to peak flux, T_{max}, and peak flux, J_{max}. The three cases of thrombin flux are shown in Fig. 7. T_{max} was set to 160 s, a time typical for onset of fibrin generation at high

concentration of $[TF]_{wall}$ (Colace *et al.*, 2012; Welsh *et al.*, 2012). The peak flux value imposed underneath the growing platelet deposit (where convection is minimal) was set to $J_{max} = 8 \times 10^{-12}$ nmole/μm^2-s, which is 10 to 100-fold less than the imposed flux needed to polymerize fibrin from flowing fibrinogen over a membrane (Neeves *et al.*, 2010). Case II deployed a five-fold reduction in J_{max} to simulate the situation of a typical low TF (~0.1/μm^2) stimulation. By testing against measured clot growth rates, Cases I and II represent predictions of the multiscale model that potentially can be compared to future measurements of thrombin generation by a growing thrombus.

While the thrombin flux condition was inspired by the CAT assay (closed system) corresponding to a partially restricted inner clot 'compartment', clot formation over collagen/TF under flow is an open system. It remains to be determined if influx of prothrombin can lead to a plateau in thrombin production. Future measurements of dynamic thrombin flux from clots formed under flow will help refine this wall flux term.

2.5 *Cell activation-driven adaptive meshing*

An important feature of platelet deposition is that the clotting region, especially at early times, occupies only a small portion of the computational domain. Consequently, using a uniform mesh throughout the entire domain incurs a large computational cost where many mesh nodes must be applied to achieve a reasonable resolution around each platelet. An adaptive meshing scheme was designed to allow the mesh density to be refined in the clotting region of an evolving rough clot surface. The mesh generator *DistMesh* (Persson & Strang, 2004) with a Gaussian size function was used to produce an unstructured triangular mesh (Figs 3 and 4). For the *i*th platelet that reached the critical activation state, we computed a 2D Gaussian, g_i, around the platelet centre:

$$g_i = \exp\left(-\frac{(x - x_i)^2 + (y - y_i)^2}{2\sigma^2}\right), \tag{3}$$

where x_i, y_i are coordinates of the centre of the *i*th platelet, σ was a parameter that describes the spread off the Gaussian in both directions. The overall influence function $G(x, y)$ was defined as the sum of all Gaussians of single platelets, i.e.

$$G(x, y) = \sum_{\text{all activated platelets}} \exp\left(-\frac{(x - x_i)^2 + (y - y_i)^2}{2\sigma^2}\right). \tag{4}$$

The size function $h(x, y)$ defined the equilibrium length of the triangular element by the Gaussian influence level as follows:

$$h(x, y) = h_{min} \quad \text{if } G(x, y) < G_{cutoff}$$
$$= \min(h_{min} + \alpha(G(x, y) - G_{cutoff}), h_{max}) \quad \text{otherwise}, \tag{5}$$

where $h(x, y)$ was the minimum equilibrium length of triangles, h_{max} was the maximum equilibrium length of triangles, α was the slope of change in the transition region and G_{cutoff} was the cut-off level for the influence.

2.6 *LKMC module*

The LKMC module was used to simulate the dynamics of platelet transport and deposition under blood flow. The LKMC simulation was executed on a square grid with lattice spacing, $h_{LKMC} = 0.5\,\mu m$, while platelets were assumed to be circular with radius (1.5 μm). Platelet transport events were defined as (i) diffusion with rate $\Gamma_D = \frac{D_{platelet}}{h^2_{LKMC}}$, where $D_{platelet}$ was the effective diffusivity accounting for both Brownian motion and the red blood cell (RBC) dispersion effect (Turitto & Leonard, 1972) and (ii) advection with rate $\Gamma_C = \frac{v_i}{h_{LKMC}}$, where v_i was the fluid velocity component along the lattice direction $\mathbf{e_i}$. The total rate of motion for each platelet was the sum of the convective and diffusive rates. This approach was validated in our earlier work (Flamm *et al.*, 2009). Flowing RBCs also generate an excess of platelet concentration in the plasma layer near the boundary, which was modelled as an additional radial drift velocity superimposed on the actual velocity that resulted in a three-fold wall excess of platelets (Eckstein & Belgacem, 1991) (Supplementary Fig. S2).

In addition to the convection–dispersion-drift events for each platelet, we also considered the activation-dependent rates of attachment and detachment between two platelets or between a platelet and the collagen boundary. Both cumulative and recent-history activation levels were considered for each platelet. The cumulative internal activation state, ξ, of the ith platelet at time t was defined as the accumulated integral calcium concentration above the basal level:

$$\xi_i(t) = \int_0^t ([Ca_i] - [Ca]_{baseline})\, d\tau, \tag{6}$$

where $[Ca]_{baseline} = 100\,nM$ (Siess, 1989). The recent-history activation level was defined as the accumulated calcium level between the current time t and previous time $t - \Delta t$ ($\Delta t = 30\,s$):

$$\xi_{\Delta t,i} = \int_{t-\Delta t}^t ([Ca_i] - [Ca]_{baseline})\, d\tau. \tag{7}$$

The recent-history activation metric allows platelet integrins to return to a resting state (non-adhesive) if calcium has returned to baseline for 30 s. One of the most widely used functional forms, the Hill functions were introduced to normalize, between $\alpha_{min} = 0.001$ and 1, the cumulative and 30-s recent history activation states:

$$F(\theta_i) = \alpha_{min} + (1 - \alpha_{min})\frac{\theta_i^n}{\theta_i^n + \theta_{50}^n}, \quad \theta_i = \xi_i,\ \xi_{\Delta t,i}, \tag{8}$$

where $\alpha_{min} = 0.001$ represents the base level of activation, n represents the sharpness of the Hill function, and θ_{50} was the critical level for 50% activation. An overall rate of attachment of the ith platelet to the collagen surface was defined by:

$$\Gamma_{att}^{collagen} = k_{att}^{collagen} F(\xi)\, F(\xi_{\Delta t,i}). \tag{9}$$

The attachment rate between the ith and jth platelet j, via fibrinogen depending on both the cumulative and transient calcium level of two particles was modelled as:

$$\Gamma_{att}^{fibrinogen} = k_{att}^{fibrinogen}\sqrt{F(\xi_i)\, F(\xi_j)}\sqrt{F(\xi_{\Delta t,i})\, F(\xi_{\Delta t,j})}. \tag{10}$$

The detachment rate between platelet and the reactive surface was modelled using the Bell exponential (Bell , 1978) to describe the shear-dependent breakage of receptor-ligand bonds,

$$\Gamma_{\text{det}}^{\text{collagen}} = k_{\text{det}}^{\text{collagen}} F\left(\xi_i\right)^{-1} F\left(\xi_{\Delta t, i}\right)^{-1} \exp\left(\frac{\gamma_i}{\gamma_c}\right), \tag{11}$$

where γ_i was the local shear rate around the ith platelet and γ_c was the characteristic shear rate required to initiate bond breakage. The detachment rate between the ith and jth platelet was given similarly by

$$\Gamma_{\text{det}}^{\text{fibrinogen}} = k_{\text{det}}^{\text{fibrinogen}} \sqrt{F\left(\xi_i\right) F\left(\xi_j\right)}^{-1} \sqrt{F\left(\xi_{\Delta t, i}\right) F\left(\xi_{\Delta t, j}\right)}^{-1} \exp\left(\frac{\gamma_i + \gamma_j}{2\gamma_c}\right). \tag{12}$$

In the current model, platelets could only dissociate as singlets from the thrombus and fracture of large chunks of platelets was not considered due to the complexity of stress propagation within the random aggregated clot. Platelets displayed no bulk aggregation as they entered the concentration boundary layer due to short exposure times and rarity of collisions in the bulk flow. Therefore, aggregation for free-flowing platelets was not considered.

At each time step, a specific event k with rate Γ_k was chosen from the rate catalogue with probability $\Gamma_k/\Gamma_{\text{total}}$. A specific time step $\tau = -\ln(u)/\Gamma_{\text{total}}$ was also chosen by drawing a random number u from the unit interval $(0, 1]$.

2.7 *Clot remodelling scheme*

Platelets can transiently roll (translocate) on Von Willebrand factor (VWF) prior to firm arrest mediated by integrin activation. However, resolving molecular-level events of detailed adhesion and restructuring mechanics incurs too much computational cost given the spatial and temporal domain of thrombosis (1000s of cells over many minutes and millimetres). A remodelling algorithm was thus designed to mimic the remodelling behaviour without providing full descriptions of the inherent biology. Upon binding, each platelet was able to roll a certain distance along the trajectory of the thrombus contour in the flow direction. A typical rolling distance of 10 μm is observed by tracking single platelet movement under microscopes. Under the square lattice settings, each platelet occupied a collection of pixelated squares in the domain. As shown in Fig. 5, whenever a quiescent platelet (in black) attempted to bind to the target platelet (in gray), a search was performed along all the potential binding sites (trajectory indicated by curved arrow) in the direction of the local flow. Upon binding, the algorithm allowed the platelet to search along the contour of the thrombus for a distance of 10 μm (observed under microscopes) based on local flow and morphology. A list of all the potential binding sites along the search trajectory and their corresponding potential binding rates were evaluated. Sites with higher binding rates are more likely to be chosen. The algorithm picks the final deposition site based the potential binding rates which are the sums of all the platelets acting on that site. For instance, a site with three neighbouring platelets (assuming all with the same activation levels, therefore same binding rates) will be three times more likely to be chosen than one with only one neighbour. Denser packing is an emergent outcome since sites that can form close packing are more likely to be chosen as these sites tend to have more platelets acting on them, thus higher potential binding rates.

This remodelling algorithm circumvented the biological complexity of detailed receptor adhesive dynamics calculations, but allowed the platelet to search for a favoured site for binding, mimicking the rolling and translocation behaviour observed both *in vitro* and *in vivo*.

2.8 *Module integration*

Exchange of information between the four computational modules was performed at specified time intervals (Supplementary Fig. S3):$\Delta t_{\text{LKMC}} = 5 \times 10^{-3}$ s, $\Delta t_{\text{LB}} = 5 \times 10^{-3}$ s, $\Delta t_{\text{FEM}} = 10^{-2}$s and $\Delta t_{\text{NN}} = 10^{-2}$s. At the start of the simulation, the LKMC, LB, FEM and NN modules were all initialized. Each module was then stepped forward in time until the first coupling time was reached ($t = 5 \times 10^{-3}$s), and then information was exchanged between relevant modules. When the total time evolved by the LKMC module first exceeded Δt_{LKMC}, each of the three modules, LB, NN and FEM was updated to the current system time. During the first update time ($\sim t = 5 \times 10^{-3}$ s), the LB solver received the current configuration of the bound platelets from the LKMC simulation and was used to update the velocity field to the current system time. Then, all methods resumed stepping forward in time until the next coupling time ($t = 10^{-2}$ s) occurred. At the time of update, all models shared information: the LKMC was used to update position of platelets in FEM, LB; LB updated the velocity field in LKMC and FEM; FEM updated the concentration field; and NN predicted the activation state of each platelet based on updated agonist concentrations to be used in LKMC and FEM. This process was repeated until the end of the specified simulation time. The overall multi-element model used 25 parameters (Table 1), the first 15 of which are either well-characterized physical or biological properties (ρ_{blood}, μ_{blood}, etc.) and the remaining 10 parameters (n, ξ_{50}, , , , , and γ_{c}) were determined from our previous model (Flamm *et al*., 2012) and experimental measurements.

3. Experimental methods

3.1 *Blood collection and preparation*

Blood was collected via venipuncture into a syringe containing 40 µg/mL of a FXIIa inhibitor CTI (Haematologic Technologies, Essex Junction, VT) from healthy donors who self-reported as free of alcohol use and had refrained from oral medication for at least 72 h prior to donation. All donors provided informed consent under approval of the University of Pennsylvania Institutional Review Board. Platelets were labelled with anti-human CD61 antibody. Fluorescent fibrinogen was added (1 mg/mL stock solution, 1:80 v/v % in whole blood) for measuring fibrin generation. All experiments were initiated within 5 min after phlebotomy.

3.2 *Preparation and characterization of collagen/TF surface*

Glass slides were treated with Sigmacote (Sigma, St. Louis, MO) to impede protein adsorption and clotting on glass surface. A volume of 5 µL of collagen was perfused through the patterning channel (250 µm wide and 60 µm high) of a microfluidic device to create a single stripe of fibrillar collagen, as previously described by Neeves *et al.* (2008) Lipidated TF was then sorbed to the collagen surface by introduction of 5 µL of Dade Innovin PT reagent (20 nM stock concentration) (Duckers *et al.*, 2010) diluted 300-, and 5-fold with N-2-hydroxyethylpiperazine-N9-2-ethanesulfonic acid buffered saline to obtain low and high TF surface concentrations of 0.1 and 10 molecules per µm², respectively, as estimated by imaging of sorbed annexin V-fluorescein isothiocyanate-stained vesicles (Zhu *et al.*, 2015). In all experiments, the Dade Innovin PT reagent was incubated with the collagen for 30 min without flow and the surface was then rinsed and blocked with 0.1% bovine serum albumin buffer.

3.3 *Microfluidic clotting assay on collagen surfaces with or without TF*

An 8-channel polydimethylsiloxane flow device (Supplementary Fig. S4), described by Maloney *et al.* (2010), was vacuum-mounted perpendicularly to collagen/TF surfaces forming eight parallel-spaced prothrombotic patches 250 µm wide by 250 µm long. Blood was then perfused across the eight channels to be withdrawn through a single outlet. Initial wall shear rate was controlled by a syringe pump (Harvard PHD 2000; Harvard Apparatus, Holliston, MA) connected to the outlet on the flow device to maintain a venous shear rate of 200 s^{-1} (corresponding to a volumetric flow rate of 2 µL/min/channel). Thrombi were formed either under constant flow rate (constant Q; CTI-treated blood in all eight channels) or under constant pressure drop (constant DP) conditions as described by Colace *et al.* (2012). To achieve constant pressure drop (pressure relief mode), EDTA-treated blood was delivered into alternating channels to abolish thrombus formation, thus allowing CTI-treated blood to clot in assay channels and divert flow into the matched EDTA channels. Platelet and fibrin activity were monitored simultaneously by epifluorescence microscopy (IX81; Olympus America Inc., Center Valley, PA). Images were captured with a charged coupled device camera (Hamamatsu, Bridgewater, NJ) and were analysed with ImageJ software (National Institutes of Health). To avoid side-wall effects, fluorescence values were taken only from the central 75% of the channel.

3.4 *Confocal imaging of clot morphology and flow rate*

Real-time clot height was determined by platelet fluorescent intensity, which was linearly proportional to the fluorescent intensity of a fully occluded thrombus. Experiments were terminated when flow was in complete cessation (full channel occlusion) in assay channels for the pressure relief condition and final clot height was assumed to be the same as the height of the channel (60 µm). Profiles of clot morphology were generated using a custom MATLAB script, in which the average of 40 vertical line-scans (in the direction of flow) was calculated. The height was also assumed to be proportional to the fluorescence level and was calibrated by the maximum intensity for a fully occluded thrombus. Supplemented fluorescent fibrinogen provides a fluorescent background in assay channels while EDTA channels remain dark all the time. Flow rate in assay channel was determined by measuring the width of the fluorescent portion in the middle flow plane at the merged outlet of every two paired channels at each time point and calculating the corresponded volumetric flow rate within the fluorescent portion of the channel using a custom MATLAB script with assumptions that a parabolic flow profile was fully developed.

4. Results

4.1 *Cell activation-driven adaptive meshing*

The FEM mesh for calculation of agonist transport was generated by the remeshing algorithm described in Section 5. The adaptive remeshing algorithm allowed for automatic generation of mesh configurations for any specific platelet contour shape that resulted stochastically from LKMC. Starting from an initially coarse uniform mesh over the entire 500µ $\times$ 60 µm simulation domain, the remeshing algorithm generated a highly resolved mesh in proximity to the growing thrombus contour, as required to resolve the boundary layers associated with the agonist concentrations. The equilibrium side length of the smallest triangles in the clotting region was set to 0.7 µm. For the earlier stages, the clotting region only occupied a small portion of the domain, and a mesh with no more than 8000 nodes was usually sufficient. For a fully developed thrombus, the program generated an unstructured triangular mesh with about 30,000 nodes and 50,000 triangular elements (Fig. 4b). For the same domain of 500 µm by 60 µm, using a uniform

square mesh with 1 μm spacing in both directions would require as many as 30,000 (500 × 60) nodes and 60,000 elements. Each activated 3-μm diameter platelet occupied about 30 triangular elements (side length = 0.7 μm) compared with nine elements for uniform meshing. Therefore, a three-fold increase in mesh resolution was achieved at the site of each platelet's release of ADP and TXA$_2$ while applying coarsened meshes elsewhere therefore maintaining a similar problem size. Computational power was especially focused during the early stages of clotting when only a few platelets were immobilized to the surface, with these initial events driving subsequent pattern formation. The refined regions occupied the concentration boundary layer extending up to ∼10 μm from the platelets on the outer most layer, thus coinciding with the regions where the sharp gradient change in agonist concentrations emerged from the simulation. A new mesh was generated only if the current mesh resolution for one or several activated platelets fails to reach the tolerance criteria. Over the course of one simulation, a total of 25 different meshes were used and mesh update was more frequent during the earlier development stage. The triangular elements were of high quality with appropriate aspect ratio (Supplementary Fig. S5) for stable and accurate finite element calculations. Overall, the adaptive remeshing scheme led to about 40% reduction in computational effort relative to the simulations with uniform meshes, with most of the savings occurring during the earlier stages of clotting.

While adaptive meshing is a well-established technique to increase computational efficiency, particle-activation driven remeshing (Fig. 4) will be critical to multiscale simulation of human thrombosis where the flow field spans the millimetre to centimetre length-scale range, whereas the thrombotic processes near the wall involve micron-scale boundary layer phenomena. Although the adaptive meshing technique itself does not present new physics, it allows us to probe larger domains that would otherwise be computationally prohibitive. In fact, it would be a necessity if the model were to be applied for larger vessel simulations where creation of suitable mesh would be vital to numerical computations. The approach developed also is a versatile and general automatic mesh refinement based on evolving platelet deposition patterns, which are not known *a priori* and are affected by flow and, in turn, affect the flow. The adaptive meshing approach of Equation (3)–(5) represents a tractable and robust numerical implementation between the Monte Carlo, NNs and Finite Element calculations of the multiscale model.

In future work, the mesh refinement within clots can be relaxed in regions where clot regions become inactive at longer times (full depletion of ADP, TXA$_2$ and thrombin). Even for clots that grow to mm-scale thicknesses to occlude a coronary artery, e.g. the current mesh refinement algorithm offers significant computational savings.

4.2 *Thrombin flux case studies*

To simulate thrombin generation, we imposed a time-dependent wall influx with the initiation and decaying stage parameterized by two parameters, T_{max} and J_{max}. A comparison of platelet deposition dynamics is shown in Fig. 7. For the first case representing normal physiology, after an initial lag of 60 s, platelet mass started to grow linearly to 400 s which was consistent with fluorescence measurements in experiments. A typical averaged thrombin concentration within the thrombus was found to be ∼30 nM which agrees with both experimental observations and earlier modelling work (Kuharsky & Fogelson, 2001). Platelets were able to grow a height of ∼50 μm in a typical constant blood flow simulation. Case II with five-fold reduction in maximum thrombin signal was also studied. Here, a delayed platelet accumulation was observed during the earlier lag phase. The thrombus height at 450 s of the simulation reached approximately ∼45 μm. Case III with no thrombin presence predicted a typical thrombus height of 20–30 μm which was consistent with our previous work (Flamm *et al.*, 2012).
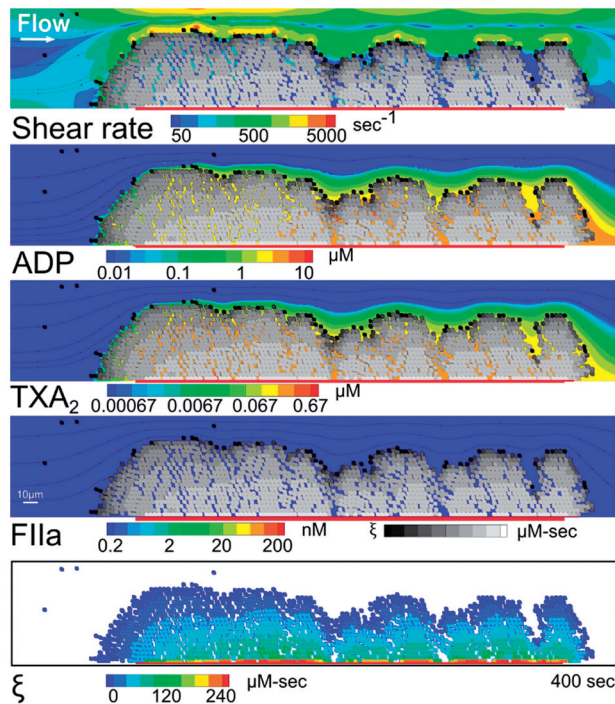
FIG. 8. Fully resolved thrombosis for whole blood flow over collagen/TF after 400 s. At constant inlet wall shear rate of 200 s^{-1}, the flow velocity becomes quite high in the narrowed lumen with peak wall shear rates exceeding $\sim$1000 s^{-1}. Platelet released ADP and TXA$_2$ and wall-derived thrombin form thin boundary layers as these species elute from the clot and are convected downstream. The simulation predicts the growth of the clot upstream of the collagen, a core of highly activated platelets in proximity with collagen, and an outer shell of relatively unactivated platelets.

Inclusion of thrombin has interesting ramifications compared to other soluble agonists. Thrombin has a diffusivity that is much lower than ADP or thromboxane. Also platelet signalling in response to thrombin displays unique properties of fast-on but slow-off due to PAR-1 and PAR-4 signalling dynamics captured in the PAS training data. Differences in calcium signalling due to thrombin (Supplementary Fig. S6) highlight these effects. Without thrombin present, a clotting event does not cause 60-micron channel occlusion or reduction of flow (Figs 8 and 9a–d). The model predicted a two-fold increase in growth rate of thrombus height ($\sim$0.13 μm/s) under the presence of thrombin as compared to the case without thrombin.

4.3 *Platelet remodelling upon deposition and thrombus morphology*

The remodelling algorithm was designed to capture platelet adhesion behaviour (VWF translocation followed by integrin mediated firm arrest) without a detailed description of single bond kinetics. In the absence of remodelling, the clot structure was found to be dendritic with dangling platelet clusters or mechanically-unlikely platelet assemblies. One of the reasons for addition of the remodelling was because the clots formed in the presence of thrombin were much larger than those studied in our prior work where thrombin was absent and dendritic growth was far less developed (Flamm *et al*., 2012).
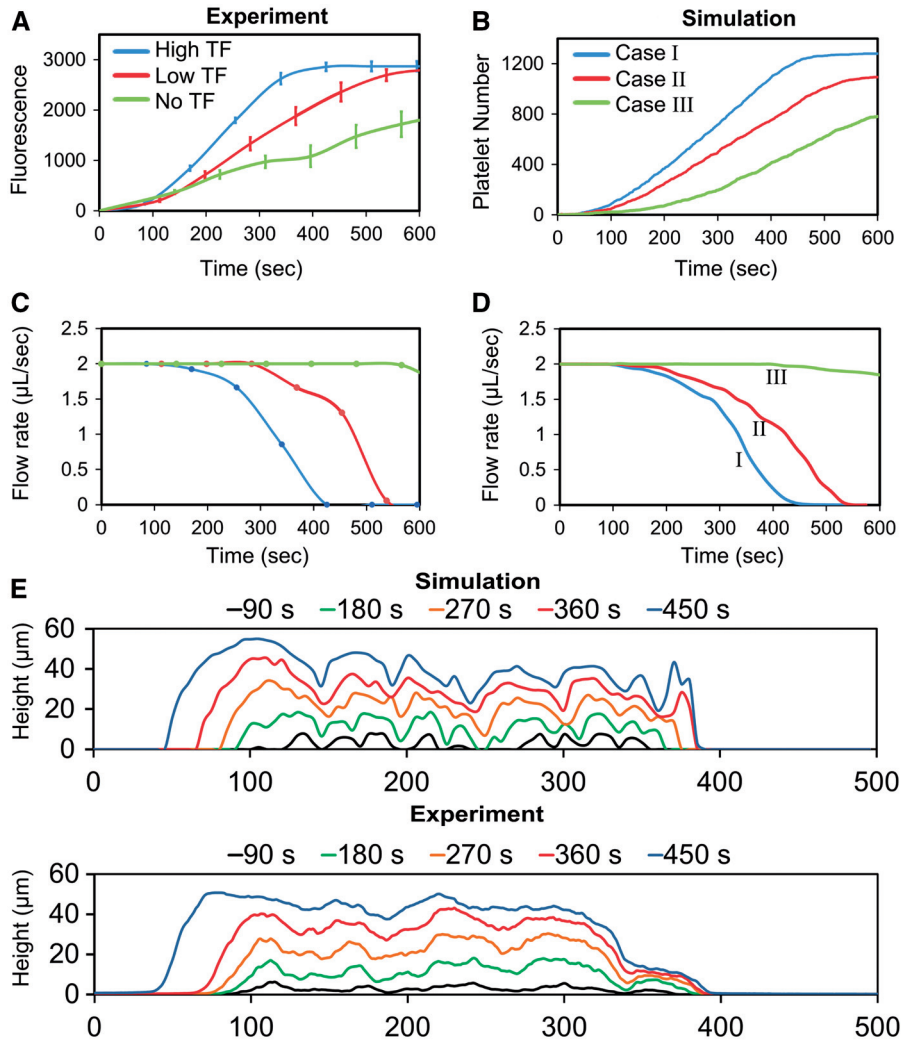
FIG. 9. Comparison of experiment (a, c) and multiscale simulation (b, d) for occlusive thrombosis. Platelet deposition (a, b) and flow rate (c, d) are shown for pressure relief mode (initial wall shear rate, 200 s^{-1}) for whole blood flow over high and low TF (10 or 0.1-molecules/μm^2). Clot morphology and clot height over collagen (located between 100 and 350 μm) is shown at various times of clotting (e: simulation, *top panel*; experiment, *bottom panel*).

The remodelling algorithm produced compact clot structures with platelet deposits that mimicked the rough modulating thrombus morphology found in experiment (Fig. 6). For an initial wall shear rate of 200 s^{-1}, the predicted rough thrombus surface grew linearly with time reaching a thickness of ∼50–60 microns in 400 s. This overall clot growth rate of ∼8 micron/min emerges from the simulation as a clinically relevant and experimentally testable metric.

The multiscale model simulated the contour evolution of platelet mass adherent to the collagen surface, the changing wall shear conditions over the rough clot, the activation and deposition dynamics of each

single platelet and the spatiotemporal concentration distribution of important agonists, ADP, TXA$_2$ and thrombin (Fig. 8, Supplementary Movie S1 and S2). The collagen surface created the initial boundary that captured the freely flowing resting platelets (note: $F(0) = \alpha_{min} = 0.001$ for resting platelets which can increase up to 1000-fold with activation). The intracellular calcium concentration rises slowly for the platelets bound to collagen but remains elevated, as driven by the NN calculator. Additionally, exposure to a strong thrombin flux enhanced activation (via PAR1/4 signalling within the trained NN calculator) for newly arriving platelets recruited to the growing deposit over the collagen. When the cumulative calcium level reached a threshold of $\xi_{crit} = 10\mu$M-s at approximately 60 s, ADP and TXA$_2$ were released forming a concentration boundary layer that worked synergistically with the thrombin in the boundary layer to strengthen the platelet calcium signalling. The concentration boundary layer thickness for ADP, TXA$_2$ and thrombin extended to 10 µm beyond the clot boundary, which was consistent with our previous work (Flamm *et al*., 2012). The ADP and TXA$_2$ concentration levels were within the effective dynamic range ($<10 \times EC_{50}$) and were significantly higher than those in the absence of the thrombin interaction in our prior work because significantly more platelets became activated. The ADP and TXA$_2$ concentrations ranged from 5 to 10 µM and 0.2 µM to 0.3 µM, respectively, in the clotting region for both constant flow and pressure relief settings.

During clotting, the agonist exposure was multicomponent and time-varying. This spatial variation in agonist exposure created three different calcium signals (Supplementary Fig. S6). For the first layer of deposition, the platelets exposed to both collagen and thrombin at the bottom surface became the most activated due to the sustained calcium mobilization induced by these two potent agonists. For the next few layers that were about 5–20 µm above the surface, the platelets were exposed to a sustained high level of thrombin stimulation especially before ADP and TXA$_2$ were produced. The calcium signal rose rapidly but decayed afterwards. For the outer most layers ($>20\,$µm above the surface), platelets were mostly exposed to high ADP and TXA$_2$ concentrations but relatively low thrombin stimulation, which was reflected in a less pronounced increase in calcium signal followed by a similar decaying process as those undergoing major thrombin influence (typically in the $5-20$ µm layer).

Another emergent feature of the simulation was that arriving platelets could facilitate growth at the front of the clot in the upstream direction (Fig. 8, Supplementary Movie S1). The accumulation of upstream platelets was consistent with experimental observation of clot growth within the microfluidic clotting assay. As platelets in the near wall layer were convected by the flow in the simulation, the approaching platelets added to the front of the immobilized platelet deposit, even in the absence of underlying collagen.

4.4 *Constant flow and pressure relief*

In both experiments and corresponding simulations, two different flow modes were considered: the constant flow rate mode and the pressure relief mode (Supplementary Fig. S2). In the constant flow rate mode, blood was perfused at a constant flow rate to ensure the initial inlet wall shear rate of 200 s^{-1} was maintained during the entire course of the experiment and simulation. This is an easily and commonly achieved experimental condition by setting a constant pump speed at the start of the experiment, but this flow mode is not physiological. There was a considerable increase in wall shear rate along the platelet-fluid boundary in the simulation. As the thrombus started to grow to the point where no more platelets could form a stable bond with the existing thrombus, the shear rate became highly variable along the thrombus contour and reached a maximum shear of about 3000 s^{-1} (a pathologically high shear rate). At ~350 s, the platelet accumulation rate was significantly reduced. At 400 s, the thrombus grew to approximately 85% occlusion with a maximum height of about 50 µm.
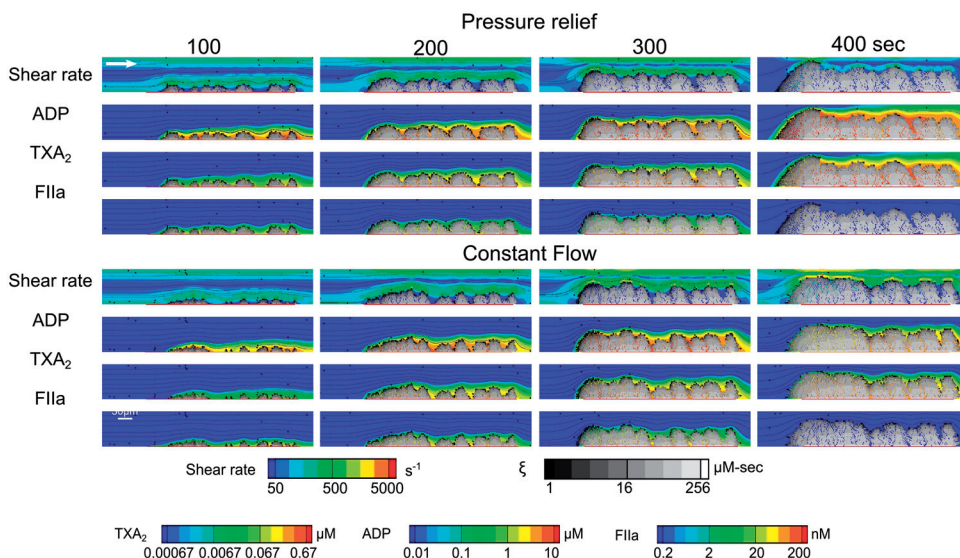
FIG. 10. Evolution over 400 s of flow and thrombosis (ADP, TXA$_2$, thrombin) under pressure relief mode (top) or at constant flow rate (bottom). Initial inlet wall shear rate = 200 s^{-1}.

However in the body, as a blood vessel becomes fully occluded, flow is diverted to other vessels. This is achieved experimentally using microfluidics in the pressure relief mode. For paired channels (one with blood treated with EDTA to quench all clotting), blood flow was diverted to the open EDTA-channel as platelets accumulated in the thrombotic active channel. Initially, the wall shear rates along the platelet-fluid boundary grew similarly as in the constant flow mode (Supplementary Fig. S7) because a partial blockage creates little pressure drop. Only at times longer than 300 s did the growing platelet mass cause a significant pressure drop and thus reduce flow in both the experiment and in the pressure relief mode simulation (Fig. 9c and d). As the channel approached full occlusion, the maximum shear rate experienced by the platelet mass was ~1000 s^{-1}, considerably less than for the constant flow rate case. Because the unbinding kinetic rates were shear-dependent [Equation (13)], the pressure relief mode allowed the platelet mass to grow to full occlusion. Another noticeable feature for the pressure relief mode was that the agonist concentration was much higher than those under constant flow settings at the later stages of aggregation. This was also expected as the flow was essentially stopped at the later stages approaching full occlusion as resistance to flow caused by the thrombus increased. With convective dilution significantly reduced, the agonist transport was mainly diffusive, leaving a much thicker boundary layer than the one with constant flow rate. We have previously observed in experiments that autocrinic effects through ADP and TXA$_2$ can be particularly potent the moment when flow stops (Muthard & Diamond, 2012), effectively leading to a flow-dependent quorum sensing mechanism.

Also, the multiscale model was able to capture platelet deposition dynamics and morphological information under different levels of TF stimulation consistent with microfluidic experiments conducted under pressure relief conditions (Figs 9 and 10). At nearly complete occlusion, a total of about 1100 and 1300 platelets were deposited on the collagen patch for 0.1 molecules/μm^2 (low) and 10 molecules/μm^2 (high), respectively, which corresponded to about 300,000 platelets in a 0.0045 μL volume [(250+50 μm)-long × 250-μm wide × 60-μm high], or ~200-fold the concentration of PRP which has a concentration of ~300,000 platelets/μL.
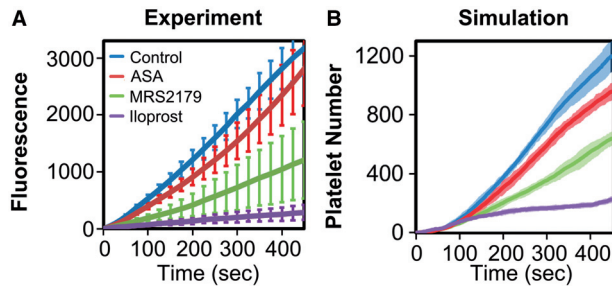
FIG. 11. Comparison of experiment (a, c, e) and multiscale simulation (b, d, f) for different agonist conditions. Measured platelet deposition in the presence of aspirin, MRS 2179 and iloprost treatment (a) and corresponding multiscale simulation ($n = 8$) with no TXA$_2$, no ADP and iloprost stimulation (b).

In both simulation and experiment, after a lag of about 50 s, the thrombus mass grew linearly from 50 to $\sim$400 s, for both high and low TF level (Fig. 9a and b). At low TF levels, a five-fold decrease in maximum thrombin flux was chosen. The typical maximum thrombin concentration (Fig. 10, Supplementary Movies S1 and S2) reached $\sim$90 and $\sim$20 nM for high and low TF cases, respectively, which was within an expected range of thrombin concentration reported for experiments (Colace *et al.*, 2012; Onasoga-Jarvis *et al.*, 2013; Zhu *et al.*, 2015). Higher levels of TF saturated the clot thrombin level. This threshold behaviour in thrombin generation was also reported in other multiscale models with coagulation cascade embedded (Kuharsky & Fogelson, 2001; Leiderman & Fogelson, 2011). For the low and high TF cases in pressure relief mode, the simulated instantaneous volumetric flow rates matched accurately with the experimental measurements (Fig. 9c and d). The multiscale model was able to predict important outcomes such as occlusion time for both low and high TF levels. Under high TF condition, the channel was occluded at around 450 s, about 100 s faster than under low TF stimulation. Individual clot morphology was also correctly predicted by the model. As seen in both simulation and experiment, the clot width extended upstream and downstream of the initial 250 μm collagen patch (Fig. 9e and f). TF level did not seem to have a substantial effect on clot morphology but did affect the thrombus growth rate. Figure 9f shows a typical 2D thrombus evolution profile under high TF condition, which compares well against the experimental height distribution averaged over a total of 40 confocal scans of the cross-section of the 3D channel (Fig. 9c). At an earlier stage of clotting, platelets were shown to form individual clumps with sizes ranging from 20 to 60 μm that were quite consistent with individual line scans.

4.5 *Agonist study*

The model was also applied to different pharmacological conditions to study the role of ADP, TXA$_2$ or prostacyclin-like signalling alters platelet deposition dynamics. In a sequence of simulations, the concentration of each agonist, ADP or TXA$_2$, was set to zero to isolate the effect of one agonist as compared to the control case. In addition, the prostacyclin analogue iloprost was set to maximum level to simulate the case of strong IP receptor stimulation. These computational conditions correspond precisely to microfluidic experiments using MRS2179 for P2Y$_1$ inhibition (removal of ADP), aspirin for COX-1 inhibition (removal of TXA$_2$) and ilopost for IP receptor stimulation. Figure 11a and b shows a comparison between the simulated platelet number and experimental fluorescence for the three agonist conditions in contrast to the control case under the low TF stimulation. Iloprost had the strongest effect by strongly inhibiting the platelet function in the experiment and in the simulation. Removing ADP also significantly

reduced platelet accumulation by almost 50% in both experiment and simulation. Inhibition of TXA_2 had the least pronounced effect, as expected for aspirin, which is a less potent antiplatelet agent. There was considerable agreement between experiments and simulations for different agonist conditions in the presence of wall generated thrombin, which represents an experimental validation of the functional forms of the adhesion dynamics which centred on the calcium signal as a metric and the thrombin wall flux used in the simulation.

5. Discussion

A major challenge in modelling blood clotting is the strong coupling of intracellular signalling, extracellular protease cascades, hemodynamics and multicomponent mass transfer. Currently, massive computational expense would be associated with: (i) single molecule resolution of adhesion dynamics, (ii) detailed bottom-up models of single platelet signalling, (iii) wall-initiated thrombin generation and (iv) complex 3D pulsatile flows. To facilitate multiscale simulation of clotting in two dimensions at reasonable computational cost, we implemented cell activation-driven adaptive meshing (Fig. 4), a rapid calculation of aggregate restructuring (Figs 5 and 6), a model of thrombin generation implemented as a boundary condition rather than as additional governing equations in the domain (Figs 1e and 2). Additionally, a data-driven NN model of platelet calcium mobilization used PAS (Figs 1e, f and 2), allowing a very rapid calculation of 'average healthy human' platelet response to multiple, time-dependent stimuli. Together, the resulting computational efficiency and the multiscale model structure using PAS-NN allows platelet phenotyping for patient-specific simulation of thrombosis. Also, the stochastic nature of the LKMC allowed the evolution of rough thrombus contours as observed in real clotting processes, a result impossible to obtain with continuum models.

The model predicted platelet calcium responses based on spatiotemporal exposures and location within the clot (Fig. 8). Platelets in contact with collagen have sustained calcium mobilization. Platelets deposited subsequently become activated to a lesser extent than the first layer of platelets with the last arriving platelets displaying the least activation driven only by eluting ADP and thromboxane (Supplementary Fig. S6). These differences in calcium signalling rate emerge from the multiscale simulation and represent tissue-scale gradients that may underlie the observed core-shell architecture observed in experiments *in vivo* in mice (Stalker *et al.*, 2014) and with human blood *ex vivo* by Welsh *et al.* (2014).

To simulate experimental studies in arterials (∼30 μm diameter) or microfluidics (60 μm channel height) with wall-derived TF, imposing a boundary flux parameterized by key parameters, maximum signal and time to reach maximum represents a suitable coarse-graining approach. Along with the aggregate restructuring model, the multiscale model predicted clot morphology (Fig. 9e), upstream clot growth (Figs 9 and 10), clot growth rate and occlusion time for the cases of high and low TF stimulation (Fig. 9a–d).

The use of apparent kinetics for cell-activation dependent binding/detachment [Equations (7)–(13)] and the platelet restructuring algorithm reduced by at least ∼10^3-fold the numerical burden of single cell/single molecule resolution via adhesive dynamics simulations. Improved resolution of concentration boundary layers over a rough boundary was achieved through the use of adaptive remeshing without a significant increase in computational burden. The remeshing algorithm used a global influence function to distinguish regions with sharp gradient change from large regions of unreactive blood flow outside the boundary layer. This feature of the remeshing algorithm will be essential for larger, 3D simulations of coronary or carotid artery thrombosis where the flow field is substantially larger and more complex. This remeshing algorithm can be readily applied to a variety of hierarchical systems biology problems

with a developing boundary layer/reaction front that is driven by discrete cell processes in the presence of prevailing transport physics.

This is the first report of a data-driven platelet model of thrombosis under flow in the presence of surface collagen/TF and convective-diffusive transport of ADP, TXA$_2$ and thrombin. Importantly, the central predictions of the simulation were tested against microfluidic experiments conducted with human blood under the exact conditions of the simulations. Two types of operational modes, constant flow and pressure relief were studied. There was considerable agreement between experimental measurements and numerical prediction on platelet morphology and thrombus formation dynamics. Clearly, clot growth rate and final size were regulated by prevailing wall shear rates. Under constant flow for constant inlet wall shear rate of 200 s^{-1}, the thrombus typically reached ~85% occlusion before the single platelet deposition on-rate was balanced by the single platelet erosion off-rate from the surface. Although the multiscale model did not treat whole-clot fracture from the surface (embolism), the steady state clot thickness of 50 μm (~85% occlusion of the 60-μm channel) occurred when the wall shear rate experienced on the clot surface exceeded ~6000 s^{-1} and the net addition of platelets was zero (*not shown*). More interestingly, the model was able to predict platelet deposition dynamics for a set of clinically relevant pharmacological conditions. One of the key features of this multiscale model was the use of intracellular calcium signalling to simulate cell–cell interactions. This signalling approach was shown to have excellent agreement with microfluidic experiments conducted on healthy donors in response to various blood modulators (Aspirin, MRS 2179, iloprost). This model has shown the ability to be used as a reliable prediction of blood function under hemodynamic conditions.

In future work of thrombosis in arterial stenoses, the effect of extreme shear rates on von Willebrand structure and function (Kumar *et al.*, 2006; Turner & Moake, 2015) will require consideration and parameterization. Additionally, numerical integration of the local instantaneous thrombin concentration provides a metric for estimating fibrin monomer generation/transport as well as fibrin formation. Fibrin, in turn, would quench platelet detachment rates. Fibrin deposition has been observed in the region closest to the TF-laden surface and to display spatial variations, typically with more fibrin appearing downstream (Colace *et al.*, 2012). In summary, flow affects clotting and clotting affects flow. The multiscale model honours this coupling by deploying data-driven kinetic information, full bottom-up reaction networks, and fully resolved hemodynamic and transport phenomenon. The computational efficiency of the algorithm is directed at supporting full simulation of thrombosis using patient-specific blood phenotypes in relevant arterial vasculatures.

Funding

Supplementary material

Supplementary material is available at http://imammb.oxfordjournals.org.

References

BABUSHKINA, E. S., BESSONOV, N. M., ATAULLAKHANOV, F. I. & PANTELEEV, M. A. (2015) Continuous modeling of arterial platelet thrombus formation using a spatial adsorption equation. *PLoS One*, **10**, e0141068.

BELL, G. I. (1978) Models for the specific adhesion of cells to cells. *Science*, **200**, 618–627.

CHATTERJEE, M. S., DENNEY, W. S., JING, H. & DIAMOND, S. L. (2010) Systems biology of coagulation initiation: kinetics of thrombin generation in resting and activated human blood. *PLoS Comput. Biol.*, **6**, e1000950.

CHATTERJEE, M. S., PURVIS, J. E., BRASS, L. F. & DIAMOND, S. L. (2010) Pairwise agonist scanning predicts cellular signaling responses to combinatorial stimuli. *Nat. Biotechnol.*, **28**, 727–732.

COLACE, T. V., MUTHARD, R. W. & DIAMOND, S. L. (2012) Thrombus growth and embolism on tissue factor-bearing collagen surfaces under flow: role of thrombin with and without fibrin. *Arterioscler. Thromb. Vasc. Biol.*, **32**, 1466–1476.

DE CATERINA, R., GIANNESSI, D., GAZZETTI, P. & BERNINI, W. (1984) Thromboxane-B2 generation during ex-vivo platelet aggregation. *J. Nucl. Med. Allied Sci.*, **28**, 185–196.

DIAMOND, S. L. (2013) Systems biology of coagulation. *J. Thromb. Haemost.*, **11** (suppl 1), 224–232.

DUCKERS, C., SIMIONI, P., SPIEZIA, L., RADU, C., DABRILLI, P., et al. (2010) Residual platelet factor V ensures thrombin generation in patients with severe congenital factor V deficiency and mild bleeding symptoms. *Blood*, **115**, 879–886.

ECKSTEIN, E. C. & BELGACEM, F. (1991) Model of platelet transport in flowing blood with drift and diffusion terms. *Biophys. J.*, **60**, 53–69.

FLAMM, M. H., COLACE, T. V., CHATTERJEE, M. S., JING, H., ZHOU, S., et al. (2012) Multiscale prediction of patient-specific platelet function under flow. *Blood*, **120**, 190–198.

FLAMM, M. H., DIAMOND, S. L. & SINNO, T. (2009) Lattice kinetic Monte Carlo simulations of convective-diffusive systems. *J. Chem. Phys.*, **130**, 094904.

FOGELSON, A. L. & NEEVES, K. B. (2015) Fluid mechanics of blood clot formation. *Annu. Rev. Fluid Mech.*, **47**, 377–403.

HATHCOCK, J., RUSINOVA, E., VAANANEN, H. & NEMERSON, Y. (2007) Lipid-bound factor Xa regulates tissue factor activity. *Biochemistry*, **46**, 6134–6140.

HOCKIN, M. F., JONES, K. C., EVERSE, S. J. & MANN, K. G. (2002) A model for the stoichiometric regulation of blood coagulation. *J. Biol. Chem.*, **277**, 18322–18333.

HOLMSEN, H., STORM, E., DAY, H. J. (1972) Determination of ATP and ADP in blood platelets: a modification of the firefly luciferase assay for plasma. *Anal. Biochem.*, **46**, 489–501.

HUBBELL, J. A. & MCINTIRE, L. V. (1986) Platelet active concentration profiles near growing thrombi. A mathematical consideration. *Biophys. J.*, **50**, 937–945.

KUHARSKY, A. L. & FOGELSON, A. L. (2001) Surface-mediated control of blood coagulation: the role of binding site densities and platelet deposition. *Biophys. J.*, **80**, 1050–1074.

KUMAR, R. A., MOAKE, J. L., NOLASCO, L., BERGERON, A. L., SUN, C., et al. (2006) Enhanced platelet adhesion and aggregation by endothelial cell-derived unusually large multimers of von Willebrand factor. *Biorheology*, **43**, 681–691.

LEE, M. Y. & DIAMOND, S. L. (2015) A human platelet calcium calculator trained by pairwise agonist scanning. *PLoS Comput. Biol.*, **11**, e1004118.

LEIDERMAN, K. & FOGELSON, A. L. (2011) Grow with the flow: a spatial-temporal model of platelet deposition and blood coagulation under flow. *Math. Med. Biol.*, **28**, 47–84.

MALONEY, S. F., BRASS, L. F. & DIAMOND, S. L. (2010) P2Y12 or P2Y1 inhibitors reduce platelet deposition in a microfluidic model of thrombosis while apyrase lacks efficacy under flow conditions. *Integr. Biol.*, **2**, 183–192.

MUTHARD, R. W. & DIAMOND, S. L. (2012) Blood clots are rapidly assembled hemodynamic sensors: flow arrest triggers intraluminal thrombus contraction. *Arterioscler. Thromb. Vasc. Biol.*, **32**, 2938–2945.

MUTHARD, R. W. & DIAMOND, S. L. (2013) Side view thrombosis microfluidic device with controllable wall shear rate and transthrombus pressure gradient. *Lab Chip*, **13**, 1883–1891.

NEEVES, K. B., ILLING, D. A. & DIAMOND, S. L. (2010) Thrombin flux and wall shear rate regulate fibrin fiber deposition state during polymerization under flow. *Biophys. J.*, **98**, 1344–1352.

NEEVES, K. B., MALONEY, S. F., FONG, K. P., SCHMAIER, A. A., KAHN, M. L., et al. (2008) Microfluidic focal thrombosis model for measuring murine platelet deposition and stability: PAR4 signaling enhances shear-resistance of platelet aggregates. *J. Thromb. Haemost.*, **6**, 2193–2201.

ONASOGA-JARVIS, A. A., LEIDERMAN, K., FOGELSON, A. L., WANG, M., MANCO-JOHNSON, M. J., et al. (2013) The effect of factor VIII deficiencies and replacement and bypass therapies on thrombus formation under venous flow conditions in microfluidic and computational models. *PLoS One*, **8**, e78732.

PERSSON, P. O. & STRANG, G. (2004) A simple mesh generator in MATLAB. *SIAM Rev.*, **46**, 329–345.

SIESS, W. (1989) Molecular mechanisms of platelet activation. *Physiol. Rev.*, **69**, 58–178.

STALKER, T. J., TRAXLER, E. A., WU, J., WANNEMACHER, K. M., CERMIGNANO, S. L., et al. (2013) Hierarchical organization in the hemostatic response and its relationship to the platelet-signaling network. *Blood*, **121**, 1875–1885.

STALKER, T. J., WELSH, J. D., TOMAIUOLO, M., WU, J., COLACE, T. V., et al. (2014) A systems approach to hemostasis: 3. Thrombus consolidation regulates intrathrombus solute transport and local thrombin activity. *Blood*, **124**, 1824–1831.

SWEET, C. R., CHATTERJEE, S., XU, Z., BISORDI, K., ROSEN, E. D., et al. (2011) Modelling platelet-blood flow interaction using the subcellular element Langevin method. *J. R. Soc. Interface*, **8**, 1760–1771.

TAYLOR, C. A., FONTE, T. A. & MIN, J. K. (2013) Computational fluid dynamics applied to cardiac computed tomography for noninvasive quantification of fractional flow reserve: scientific basis. *J. Am. Coll. Cardiol.*, **61**, 2233–2241.

TOMAIUOLO, M., STALKER, T. J., WELSH, J. D., DIAMOND, S. L., SINNO, T., et al. (2014) A systems approach to hemostasis: 2. Computational analysis of molecular transport in the thrombus microenvironment. *Blood*, **124**, 1816–1823.

TOSENBERGER, A., ATAULLAKHANOV, F., BESSONOV, N., PANTELEEV, M., TOKAREV, A., et al. (2016) Modelling of platelet-fibrin clot formation in flow with a DPD-PDE method. *J. Math. Biol.*, **72**, 649–681.

TURITTO, V. T. & LEONARD, E. F. (1972) Platelet adhesion to a spinning surface. *Trans. Am. Soc. Artif. Intern. Organs*, **18**, 348–354, 358.

TURNER, N. A. & MOAKE, J. L. (2015) Factor VIII is synthesized in human endothelial cells, packaged in weibel-palade bodies and secreted bound to ULVWF strings. *PLoS One*, **10**, e0140740.

WELSH, J. D., COLACE, T. V., MUTHARD, R. W., STALKER, T. J., BRASS, L. F., et al. (2012) Platelet-targeting sensor reveals thrombin gradients within blood clots forming in microfluidic assays and in mouse. *J. Thromb. Haemost.*, **10**, 2344–2353.

WELSH, J. D., STALKER, T. J., VORONOV, R., MUTHARD, R. W., TOMAIUOLO, M., et al. (2014) A systems approach to hemostasis: 1. The interdependence of thrombus architecture and agonist movements in the gaps between platelets. *Blood*, **124**, 1808–1815.

WU, Z., XU, Z., KIM, O. & ALBER, M. (2014) Three-dimensional multi-scale model of deformable platelets adhesion to vessel wall in blood flow. *Philos. Trans. A Math. Phys. Eng. Sci.*, **372**, 20130380.

XU, Z., CHEN, N., KAMOCKA, M. M., ROSEN, E. D. & ALBER, M. (2008) A multiscale model of thrombus development. *J. R. Soc. Interface*, **5**, 705–722.

XU, Z., KIM, O., KAMOCKA, M., ROSEN, E. D. & ALBER, M. (2012) Multiscale models of thrombogenesis. *Wiley Interdiscip. Rev. Syst. Biol. Med.*, **4**, 237–246.

XU, Z., LIOI, J., MU, J., KAMOCKA, M. M., LIU, X., et al. (2010) A multiscale model of venous thrombus formation with surface-mediated control of blood coagulation cascade. *Biophys. J.*, **98**, 1723–1732.

ZHU, S., TRAVERS, R. J., MORRISSEY, J. H. & DIAMOND, S. L. (2015) FXIa and platelet polyphosphate as therapeutic targets during human blood clotting on collagen/tissue factor surfaces under flow. *Blood*, **126**, 1494–1502.

ZOU, Q. S. & HE, X. Y. (1997) On pressure and velocity boundary conditions for the lattice Boltzmann BGK model. *Phys. Fluids*, **9**, 1591–1598.